FLUID FLOW AND INCLUSION MOTION IN THE CONTINUOUS CASTING STRAND

Lifeng Zhang (Dr.), Brian G. Thomas (Prof.),
140 Mech. Engr. Bldg., MC-244, 1206 W. Green St.
Univ. of Illinois at Urbana-Champaign
Urbana, IL61801, U.S.A.
Tel: 1-217-244-4656, Fax: 1-217-244-6534
zhang25@uiuc.edu, bgthomas@uiuc.edu

ABSTRACT

Turbulent flow and the transport and removal of inclusions in the strand of the continuous slab caster are investigated using computational models, and validated through comparison with plant measurements of inclusions. Steady 3-D flow of steel in the liquid pool in the mold and upper strand is simulated with a finite-difference computational model using the standard k-ε turbulence model in the CFD code, Fluent. Inclusion trajectories are calculated by integrating each local velocity, considering its drag and buoyancy forces. A "random walk" model is used to incorporate the effect of turbulent fluctuations on the particle motion. The predicted inclusion locations and removal fractions are compared with measured inclusion locations, amounts, size distribution, and total oxygen contents between tundish and slab. The effect of SEN outport angle and steps on fluid flow, inclusion motion and removal is studied.

INTRODUCTION

Increasing the productivity and improving the product quality are permanent requirements concerning the continuous casting process. Plant observations have found that many serious quality problems, including inclusion entrapment, are directly associated with the flow pattern in the mold. [1)] Thus design and control of the fluid flow pattern in the continuous casting mold to remove inclusions is of crucial importance to the steel industry. The flow pattern in the mold can be controlled by many variables, including the nozzle and mold geometry, submergence depth, steel flow rate, argon injection rate, electromagnetic stirring, and flux layer properties. Nozzle technology is an easy and inexpensive way to optimize the fluid flow in the mold. New techniques involving the Submergence Entry Nozzle (SEN) to improve the fluid flow pattern and inclusion removal includes swirl nozzle technique[2-5)], step nozzle technique[6-10)], multiports nozzle[11)], and oval offset bore throttle plate[12, 13)]. The fluid flow in the continuous casting mold can be investigated by mathematical modeling[14-20)], physical modeling[21-30)], or industrial trials[31-33)]. Mathematical modeling is an effective, inexpensive tool to get information that cannot be directly measured in the steel.

Two main approaches have been applied to model the behavior of the second phase particles in continuous casting: the simple convective-diffusion approach[14, 34-40)] and full trajectory calculations[40-45)]. The convective-diffusion approach employs an equation to calculate the particle concentration, which

is the same as the solute transport equation[18] except adding the terminal rising velocity of the particle to the longitudinal velocity of liquid. The full trajectory calculations solve a transport equation for each particle as it travels through the calculated fluid flow velocity field. Different researchers used different particle velocity equations. [41, 43, 44]

In the current first studies industrial measurements of inclusions in steel from the tundish to the slab are described, then the steady flow in the strand of the continuous caster is simulated with a 3-D finite-difference computational model using the standard k-ε turbulence model in Fluent [46]. Inclusion trajectories are calculated by integrating each local velocity, considering its drag and buoyancy forces. A "random walk" model is used to incorporate the effect of turbulent fluctuations on the particle motion. Thirdly The effect of steps in SEN on the fluid flow and particle motion in the mold is investigated.

MATHEMATICAL MODEL OF FLUID FLOW AND INCLUSION MOTION

The continuity equation and Navier-Stokes equations for the steady fluid flow of incompressible Newtonian fluids are

$$\frac{\partial}{\partial x_i}(\rho u_i) = 0 \ , \tag{1}$$

$$\frac{\partial}{\partial x_i}(\rho u_i u_j) = -\frac{\partial P}{\partial x_i} + (\mu_o + \mu_t)\frac{\partial}{\partial x_j}\left(\frac{\partial u_i}{\partial x_j} + \frac{\partial u_j}{\partial x_i}\right) + \rho g_i + F_j \ , \tag{2}$$

where ρ, liquid density (kg/m^3); u_i, velocity component in x_i direction (m/s); P, pressure field (N/m^2); μ_o, laminar viscosity (kg/m-s); μ_t, turbulence viscosity (kg/m-s); g_j, magnitude of gravity in j direction (m/s^2); F_j, other body forces (eg. from eletromagnetic forces); i, j, coordinate direction indices, which when repeated in a term, implies the summation of all three possible terms.

With the k-ε Model [20, 47], the turbulent viscosity is given by

$$\mu_t = \rho C_\mu \frac{k^2}{\varepsilon} \ , \tag{3}$$

where C_μ ,empirical constant = 0.09; k, turbulent kinetic energy field, m^2/s^2; ε= turbulent dissipation field, m^2/s^3. The two additional partial differential equations for the transport of turbulent kinetic energy and its dissipation rate are given by:

$$\rho u_j \frac{\partial k}{\partial x_j} = \frac{\partial}{\partial x_j}\left(\frac{\mu_t}{\sigma_K}\frac{\partial k}{\partial x_j}\right) + \mu_t \frac{\partial v_j}{\partial x_i}\left(\frac{\partial u_i}{\partial x_j} + \frac{\partial u_j}{\partial x_i}\right) - \rho\varepsilon \ , \tag{4}$$

$$\rho v_j \frac{\partial \varepsilon}{\partial x_j} = \frac{\partial}{\partial x_j}\left(\frac{\mu_t}{\sigma_\varepsilon}\frac{\partial \varepsilon}{\partial x_j}\right) + C_1 \mu_t \frac{\varepsilon}{K}\frac{\partial u_j}{\partial x_i}\left(\frac{\partial u_i}{\partial x_j} + \frac{\partial u_j}{\partial x_i}\right) - C_2 \frac{\varepsilon}{K}\rho\varepsilon \ , \tag{5}$$

where $\partial/\partial x_i$, differentiation with respect to coordinate direction x,y, or z (m); σ_K, σ_ε, empirical constants (1.0, 1.3); C_1, C_2, empirical constants (1.44, 1.92). The k-ε Model needs special "wall functions" as boundary conditions, in order to achieve reasonable accuracy on a coarse grid. [46]

The trajectory of each particle can then be calculated incrementally by integrating its local velocity. The local velocity of inclusions is represented by Eq.(6) considering the force balance between drag force and the gravitational force.

$$\frac{du_{pi}}{dt} = \frac{3}{4}\frac{1}{d_p}\frac{\rho}{\rho_p}C_D\left(u_{pi} - u_i\right)^2 - \frac{\left(\rho - \rho_p\right)}{\rho_P}g_i \tag{6}$$

where ρ_P, ρ, the particle and liquid densities, kg/m^3; $u_{p,i}$, the particle velocity, m/s; C_D, the drag coefficient as a function of particle Reynolds number, given as below

$$C_D = \frac{24}{\mathrm{Re}_p}\left(1 + 0.186\,\mathrm{Re}_p^{0.653}\right). \tag{7}$$

A "random walk" model is used to incorporate the effect of turbulent fluctuations on the particle motion. In this model, particle velocity fluctuations are based on a Gaussian-distributed random number, chosen according to the local turbulent kinetic energy. The random number is changed, thus producing a new instantaneous velocity fluctuation, at a frequency equal to the characteristic lifetime of the eddy. The instantaneous fluid velocity can be represented by

$$u = \bar{u} + u', \tag{8}$$

$$u' = \xi\sqrt{\overline{u'^2}} = \xi\sqrt{2k/3} \tag{9}$$

where u : the instantaneous fluid velocity, m/s; $\bar{u}$: the mean fluid phase velocity, m/s; u': random velocity fluctuation, m/s; ξ: the random number.

As boundary conditions for the particle motion, particles escape at the top surface and the open bottom, are reflected at symmetry plane, and are entrapped when they touch wide faces and narrow faces which represent the dendritic solidification front. . This trapping boundary condition is valid for particles smaller than the primary dendrite arm spacing and has been employed by several researchers [35, 36, 42]. However, particles touching the solidifying front are not always engulfed. The entrapment phenomenon is very complex and is receiving well-deserved attention in recent work.[37-39] The parameters of the SEN and the caster are shown in **Tables 1** and **2**.

Table 1. Parameters of the SEN

Parameters	Value
SEN bore diameter, length (mm)	80, 1292
SEN submergence depth (mm)	300
Port width × port height (mm×mm)	65 ´ 80
Port thickness (mm)	30
Port angle	Down 15 deg, up 15 deg, zero deg
Bottom well depth (mm)	10
Liquid steel flow rate (m^3/s)	0.0065
Casting speed (m/min)	1.2
Fluid density (kg/m^3)	7020
Fluid kinetic viscosity (m^2/s)	9.54×10^{-7}
Particle size (diameter) (μm)	49, 225
Particle density (kg/m^3)	5000
Inlet condition	From the simulation of tundish outlet
Inclusion motion model	Random-Walk, 0.001s time step, 10000 particles each size
Turbulence	k-e two equation, Fluent

Table 2. Parameters of the caster

Parameters	Value
Inlet port size (width×height) (m×m)	0.065×0.080
Nozzle angle	Down 15o, up 15o, zero
Submergence depth (m)	0.3
Domain height/width/thickness (m)	2.55/1.3/0.25
Average inlet flow rate (half mold) (m^3/s)	0.00325
Casting speed (m/min)	1.2
Fluid density (kg/m^3)	7020
Fluid kinetic viscosity (m^2/s)	0.954×10^{-6}
Particle density (kg/m^3)	5000
Particle diameter (μm)	49, 225
Inlet condition	Nozzle simulation result
Gas flow rate	None
Turbulence model	k-ε, by Fluent
Inclusion motion model	Random walk model, Fluent, 80 tries, 16000 inclusions
Boundary condition for inclusions	Escape from top surface and open bottom, trapped at narrow and wide face walls

INDUSTRIAL TRIALS OF INCLUSION MEASUREMENTS

Industrial trials were carried out at Baosteel (P.R.China) and reported previously [48]. A brief summary is provided here. Low carbon Al-killed steel samples taken at tundish, mold, and different places in the slab. Tundish steel samples from 300mm above its outlet, and mold steel samples from 150mm below the meniscus and 300mm away from the SEN outport.

The measured total oxygen distribution along the slab thickness is shown in **Fig.1**. The total oxygen in the slab is 10-32ppm, averaging 24 ppm. Slight peaks are sometimes found at the centerline and occasionally at the inner radius half thickness of the slab.

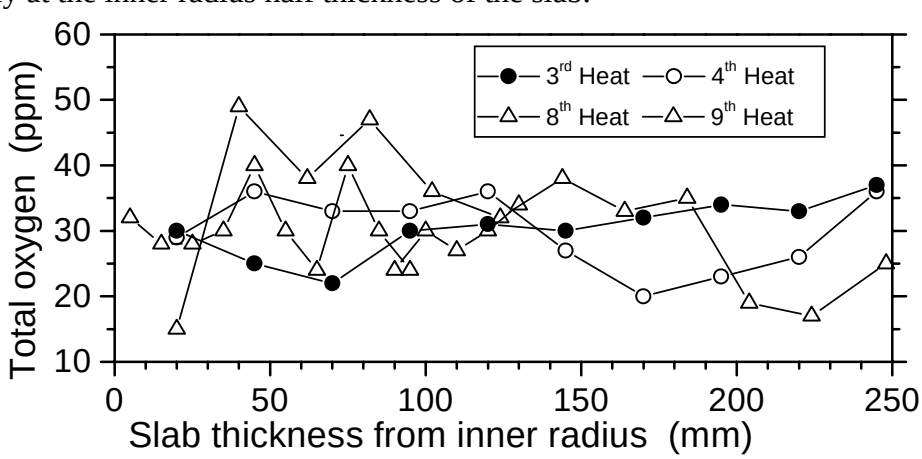

Fig.1 The distribution of the total oxygen, sulfur, phosphorus, and carbon along the slab thickness

The distribution of inclusions along the slab thickness measured from microscope observations is shown in **Fig. 2**, which suggests that: 1). Inclusions concentrate more in the 20mm thickness nearest the slab surface; 2). Some slabs have occasional accumulation at the ½ and the ¼ slab thickness from the inner radius; 3). Filters in the tundish are effective at lowering microinclusion levels. Further

investigation indicates that this inclusion accumulation is more prevalent in places such as the slab head and tail cast during unsteady conditions, as shown in **Fig.3**, from sulfur print detection. Microscope observation and SEM detection suggest that this inclusion accumulation is mainly induced by the entrapment of dislodged clogged materials from the SEN during the ladle change. Slag inclusions are mainly entrapped at the surface of the slab, as shown in **Fig.4**

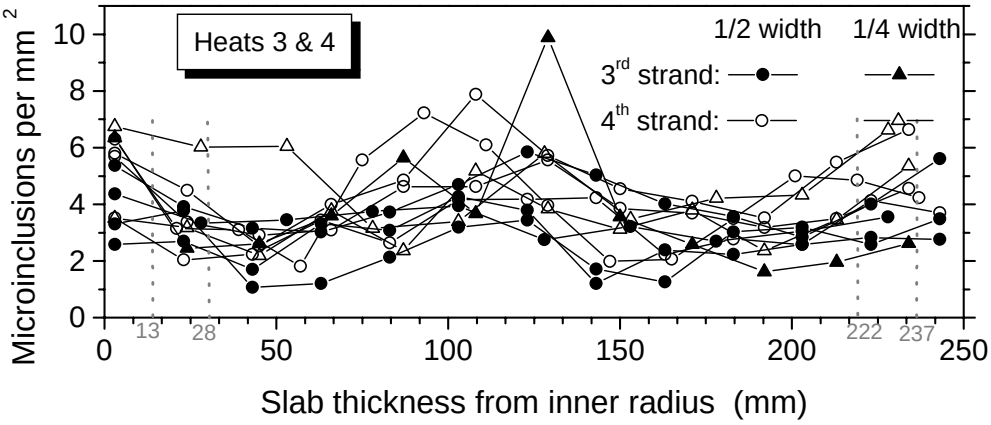

Fig.2 Inclusions distribution (<50μm) along the slab thickness with (strand 3) and without (strand 4) tundish filters

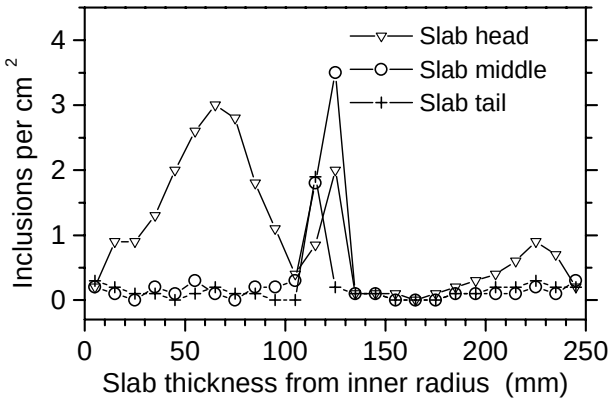

Fig. 3 Inclusion distribution along the slab thickness by sulfur print detection

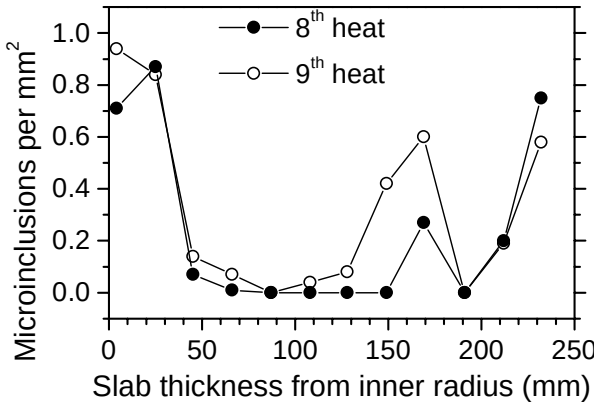

Fig.4 Slag inclusion distribution along the slab thickness by microscope observation

(a) (b) (c) (d) (e)

Fig.5 Typical inclusions observed by microscope in the mold (a,b) and slab (c,d,e) (a and b: microscope observation; c,d,e: Slime test)

The morphology, composition and possible sources of typical inclusions found in steel samples of mold and slab are shown in **Figs 5**. The morphologies include: i) angular aluminate (Fig.5b,d,e); ii) alumina cluster (Fig.5c); and iii) spherical silicate (Fig.5a). The possible sources are deoxidation products, reoxidation product, slag entrapment or broken refractory lining bricks.

Figure 6 is the inclusion number per unit 2-dimensinal section area by microscopic observation, with a large variable histogram "bin" size. Inclusions extracted by Slimes test were suspended in water and their size distributions measured with a Coulter counter to get a 3-dimentional inclusion size distribution. This obtained the 3-dimensional size distribution up to 62μm. The curves were extrapolated to around 120μm as given in **figure 7** by matching to the measured amount of extracted inclusions larger than 50μm. The inclusions mass fraction is 66.8ppm in the tundish, 57.7ppm in the 20mm thickness nearest the slab surface, and averaging 51.9ppm in the slab. This suggests that inclusions in the interior of the slab (i.e., except outer 20mm thickness of the slab) is 50.6ppm. The fraction of inclusions removed from tundish to slab is around 22%.

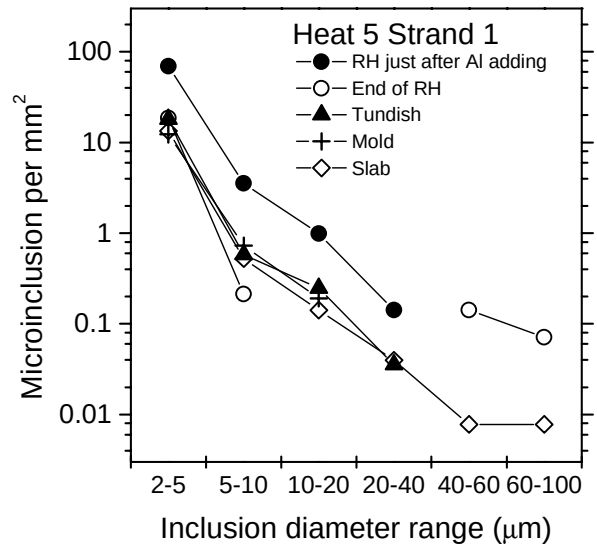

Fig.6 Microinclusion size distribution by the microscope observation

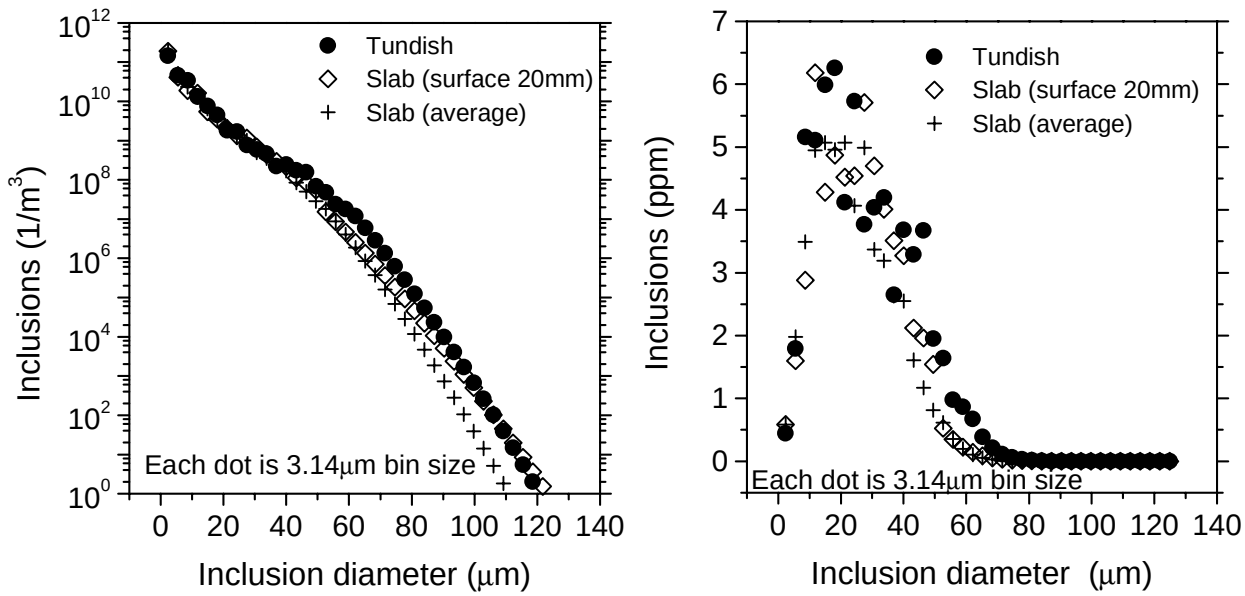

Fig. 7 Inclusion size distribution evolution by Coulter Counter measurement of the Slime extracted inclusions

COMPARISON OF INCLUSION REMOVAL BETWEEN SIMULATION AND INDUSTRIAL MEASUREMENTS

Computed locations of inclusions that attach to the SEN walls and are entrapped at the wide faces of the slab are shown in **figure 8**. The calculation suggests that around 12% of the inclusions leaving the tundish stick to the SEN walls (removed by clogging). Fig.8 suggests roughly uniform buildup on the nozzle walls, with increased tendency towards buildup on the SEN bottom due to impact from the flowing jet. This is consistent with observations of nozzle clogging where local reoxidation or chemical interaction were not the cause. **Table 3** compares inclusion fractions entrapped at different

destinations with the industrial measurements. For inclusions smaller than 50 μm entering the mold, only 7% are safely removed by the top surface (6% from tundish to slab in Table 5), independent of inclusion size. A larger fraction of inclusions bigger than 50 μm are removed. The majority of inclusions leaving the tundish (more than 60%) are captured within 30mm of the surface, which represents the top 2.55m of the caster. Fig. 8 also shows that inclusions accumulate peaks are at 12-14mm below the surface of the slab. This agrees only qualitatively with measurements in Fig. 2,3,4. A disproportionately large fraction of these (15-16%) are captured in the narrow face, despite its smaller surface area, owing to the jet impingement against its inner solidification front. Inclusions exiting the domain are entrapped somewhere deeper in the interior than 30mm shell thickness. If the entrapment criteria are the same for small and large inclusions, their entrapment to walls is very similar at 0-30mm slab surface thickness. Only 3-12% of the inclusions entering the mold are predicted to be removed by the top surface (2.6-11% from tundish to slab in Table 3). Adding 12% sticking to the SEN walls as clogged material, the simulated inclusion removal from tundish to slab is 18-23%, which agrees well with the measurement of 22% from Fig. 7.

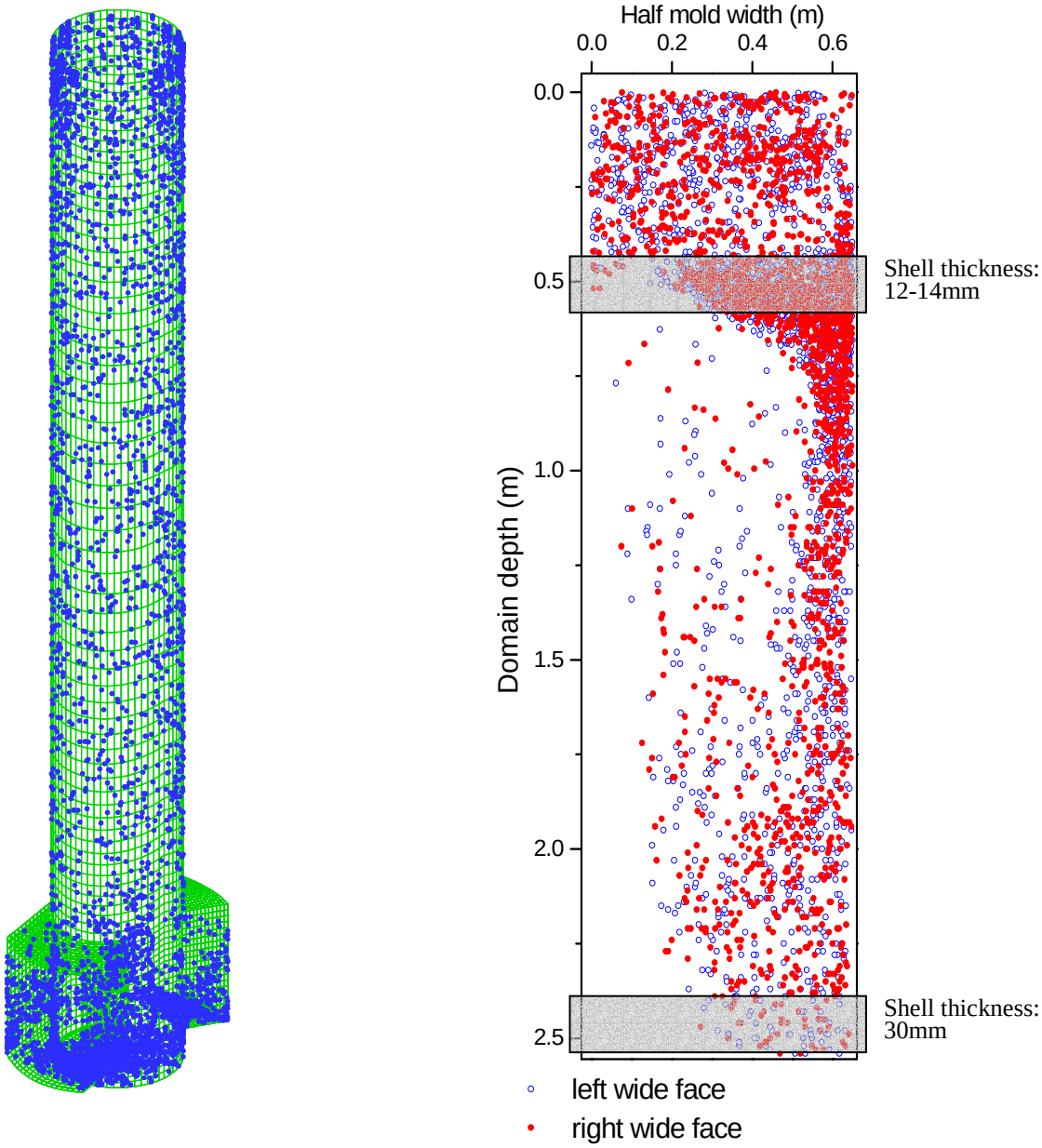

Fig.8 Inclusion locations sticking to SEN walls (left) and to the half wide faces of the slab (right)

Table 3. Fractions of inclusions entrapped at different locations after leaving tundish

	Size	SEN walls	Top slag of mold	Slab		
				Narrow face	Wide face	Interior
Simulation				0-30mm	0-30mm	30-125mm
	50μm	**12%**	**2.6-6.9%**	15-16%	40-43%	15-28%
	225μm	**12%**	**11%**			
Measurement	All	**22%**	(decrease from tundish to slab)			

EFFECT OF SEN PORT ANGLE AND STEPS

Fluid Flow Results

The dimensions of a conventional SEN and an SEN with two annular steps (Step SEN) and the fluid flow pattern are shown in **figure 9**. Due to the sharp decreasing of the bore diameter at the steps, the fluid flow is accelerated at these locations in the Step SEN. This acceleration helps to diminish the non-uniform velocities generated by the slide gate as shown in Fig.9. Without steps, the uneven flow passing the slide gate finally generates a swirl at the bottom of the nozzle, therefore the molten steel enters mold with swirl.

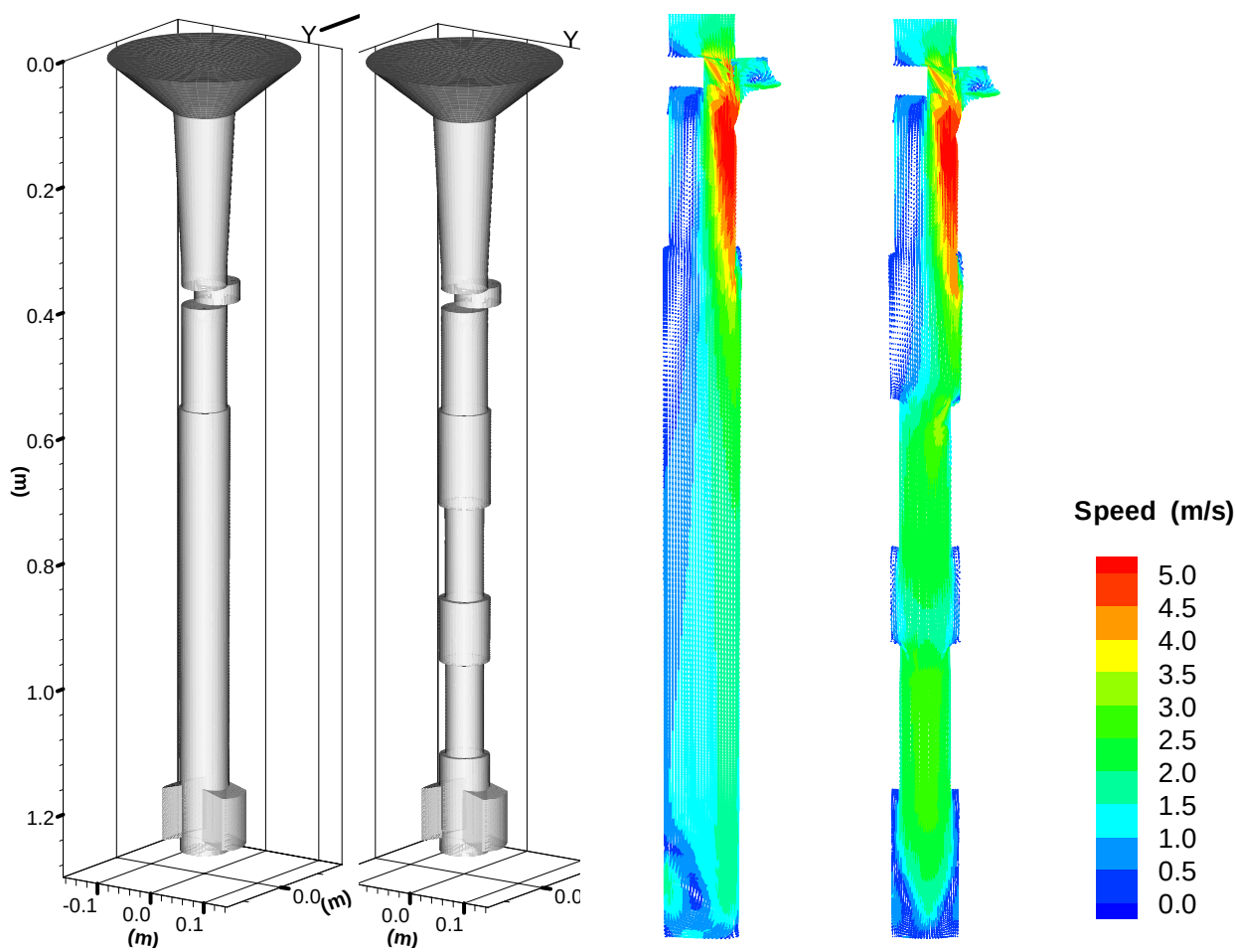

Fig. 9 Dimensions of conventional SEN and Step SEN and fluid flow pattern inside

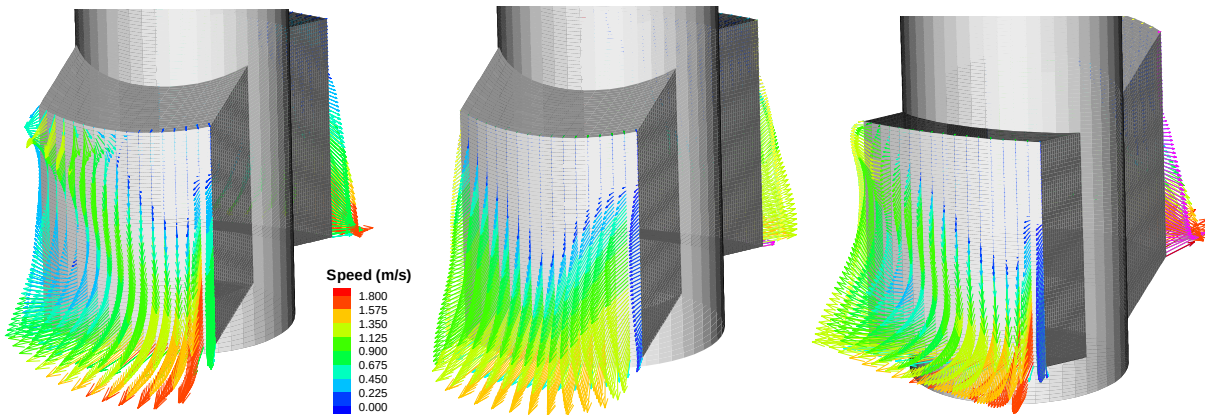

Fig. 10 Flow pattern at outports of down 15° angle without steps (left), down 15° angle with steps (middle), up 15° angle without steps (right)

This swirl at the bottom and outports are diminished in the Step SEN (**figure 10**). Jet characteristics for nozzles with outports angle of 15° down, 0° horizontal, 15° up, and Steps are compared in **Table 4**. The 15° down nozzle with two steps has the smallest turbulent energy and dissipation rate, which means the jet entering the mold has the weakest turbulence. The jet angle is only 18° for the Step SEN (Down 15°), compared with 29° without steps (Down15^o), and 18° for Zero degree angle nozzle without Steps. The large jet angle corresponds to a large impingement depth, therefore worsens the inclusion removal to the top surface. One problem of the Step SEN is its large back flow zone fraction, 30%, compared with all three conventional nozzles in Table 4. Larger back-flow zone will bring more inclusions back to the outport region of SEN, possibly inducing clogging there.

Table 4 Jet characteristics of SEN with different outports angle and steps in nozzle

SEN Outport angle	Down 15	Down 15	Zero	Up 15
With steps or not	No	Two Steps	No	No
Weight average x velocity (m/s)	0.80	0.96	0.87	0.86
Weight average y velocity (m/s)	-0.0351	0.012	0.0018	-0.007
Weight average z velocity (m/s)	0.45	0.32	0.14	0.28
Weight average turbulent energy (m^2/s^2)	0.27	0.20	0.32	0.31
Weight average turbulent energy dissipation rate (m^2/s^3)	6.41	5.27	10.47	8.88
Vertical jet angle (^{o})	29.29	18.23	9.10	17.76
Horizontal jet angle (^{o})	-2.52	0.72	0.12	-0.47
Jet speed (m/s)	0.92	1.01	0.89	0.90
Back-flow zone fraction (%)	15.31	29.38	26.15	20.73
With swirl or not at Outports	With	No	With	With

The velocity vector distribution on the center face of the mold with different SEN configurations (Table 3) are shown in **figure 11**. All four cases have a double roll flow pattern. The upper loop reaches the meniscus and may cause the increase in surface height near the narrow face for these conditions of deep 300mm submergence and no gas injection. The second loop takes steel downwards into the liquid core and eventually flows back towards the meniscus in the strand center. However, the impingement point on the narrow face and the jet penetration depth is different. Without steps (Fig.10 a), the penetration depth is deeper than with steps (Fig.11b). The steepest nozzle angle naturally produces the deepest penetration depth. **Figure 12** shows the speed along three vertical lines on the center face, indicating the different peak positions for these different nozzles.

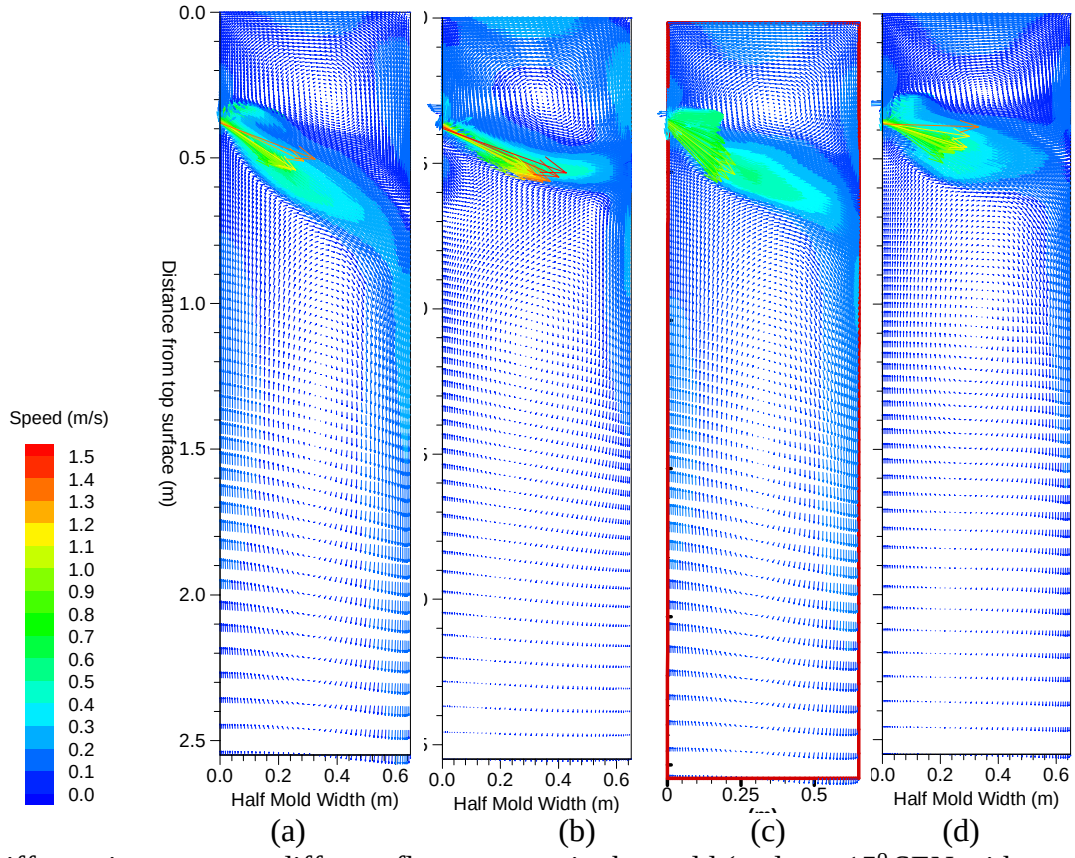

Fig.11 Different jets generate different flow patterns in the mold (a: down 15° SEN without steps; b: down 15° SEN with steps, c: 0° SEN without steps; d: up 15° SEN without steps)

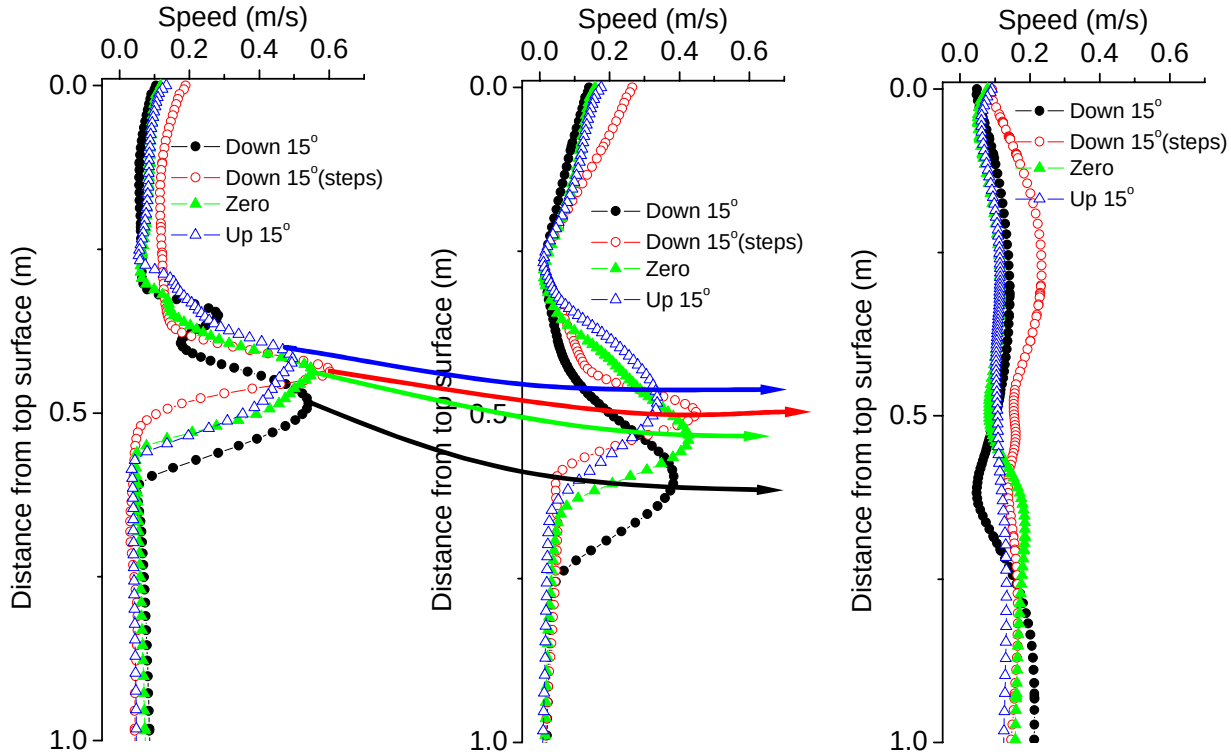

Fig.12 Speed at lines 0.15m (left), 0.325m (middle), and 0.6 m (right) away from the center of SEN on the central face of half mold.

Figure 13 shows the streamlines on the center face of the mold induced by these four different SENs. It clearly shows that annular steps in the SEN decreases the penetration depth. The eye of the lower loop with steps is higher than without.

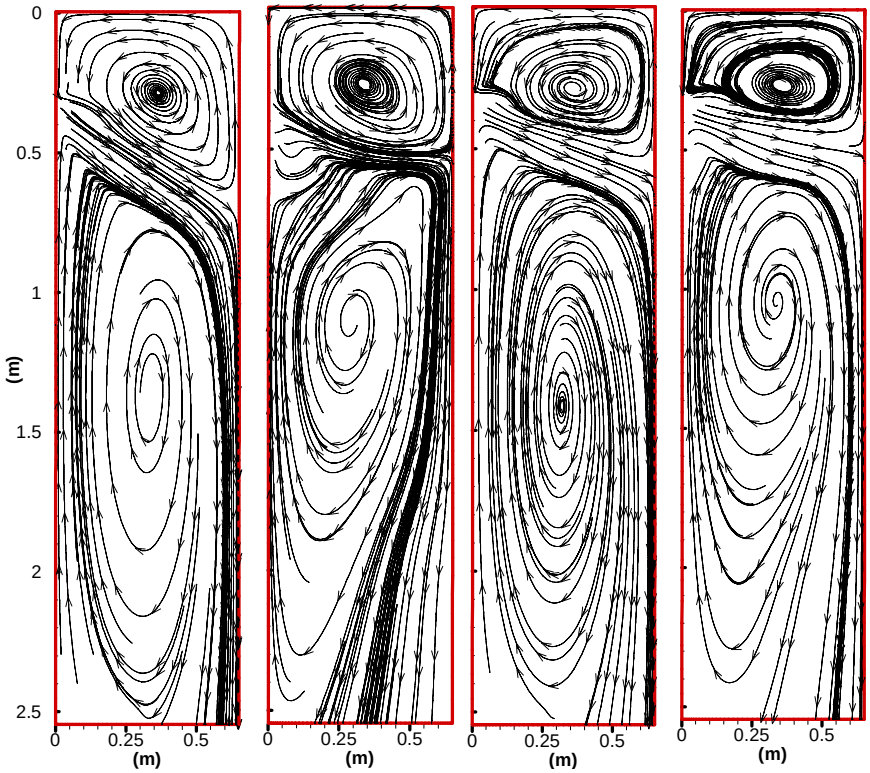

(a) (b) (c) (d)

Fig.13 Different jets generate different streamlines in the mold (a) 15° down SEN without steps; (b) 15° SEN down with steps; (c) 0° SEN without steps; (d) 15° up SEN without steps)

Inclusion Transport and Removal Results

Fractions to different destinations of inclusions entering the mold are shown in **Table 5**. The shell thickness depends on solidification time according to the following equation [49)]

$$S = 2.82t^{0.5} - 0.76\,, \tag{10}$$

where S is the shell thickness in mm, t is the time in seconds. For the current domain length 2.55m, and the current casting speed 1.2m/min (0.02m/s), the shell thickness at the open bottom of the domain is around 30mm. 31.4% of the 50 μm inclusion will be entrapped in the central region of the slab (30-125mm thick) using the non-step 15° down nozzle. This number decreases to 15.7% for the stepped 15° down nozzle, 17.1% for zero angle nozzle, and 29.4% for 15° up nozzle.

Table 5 Fractions in percentage to different destinations, and average residence times before reaching different destinations of inclusions entering the mold

	Fractions to different destinations (%)						Average residence times (s)				
	Top	Wide1	Wide2	Narrow	Bottom		Top	Wide1	Wide2	Narrow	Bottom
Down15^o	2.9	20.5	27.5	17.6	31.4		23.7	23.9	22.5	13.5	25.9
Down15^o (Steps)	6.9	28.9	30.3	18.2	15.7		11.1	23.6	26.1	13.0	49.1
Zero	5.1	23.5	35.8	18.4	17.1		22.7	26.7	20.4	14.8	31.7
Up15^o	2.8	20.4	28.0	19.3	29.4		21.7	41.7	33.3	19.5	54.5

The step nozzle may have more inclusion removal to the top surface of the mold perhaps by eliminating swirls at SEN outports and in the mold, and deceasing the impingement depth of the jet in

the mold. For the down 15° angle nozzle, only 3% of the inclusions are removed to the top surface, but this number increases to 7% with two annular steps. Table 5 also shows a disproportionate number of inclusions are entrapped by the narrow faces (18%) compared with the wide faces (50-60%). From the average residence time of inclusions before being entrapped, positions of inclusions accumulation peaks near the surfaces of the slab can be calculated with Eq.(10), which indicates that inclusions accumulate at 12-14mm below wide surfaces, and 9-10 below narrow surfaces. Because the inclusion removal rates are so small for all nozzles, it is more important to choose nozzle designs that produce optimal conditions at the meniscus to avoid slag entrainment, level fluctuations, and other problems.

SUMMARY

1. The typical morphologies of inclusions in the continuous casting slab are angular aluminate, alumina cluster, and spherical silicate. The possible sources are deoxidation products, reoxidation product, slag entrapment or broken refractory lining bricks.

2. Measurement indicates that trapped inclusions concentrate mostly within 20mm of the slab surface. Some slabs have occasional concentration at the ¼ slab thickness from the inner radius, mainly induced by the entrapment of released clogged materials from the SEN during ladle exchanges.

3. In the continuous caster, around 12% of inclusions leaving the tundish are removed by sticking to the SEN walls, and only 3-11% are predicted to be removed to the top slag of the mold. This roughly matches the measured total inclusion removal fraction to the top surface of 22%. The majority of simulated inclusions entering the mold (60%) are captured within 30mm of the surface of the slab, which represents the top 2.55m of the caster. Simulation indicates that inclusion accumulation peaks are at 12-14 mm below the surface of the wide face, which agrees well with the measurement.

ACKNOWLEDGEMENTS

The authors are grateful for support from the National Science Foundation (Grant No. DMI-0115486), the Continuous Casting Consortium and the National Center for Supercomputing Applications at the University of Illinois. The authors also wish to thank Baosteel, University of Science and Technology Beijing, and the Central Iron and Steel Institute (P.R.China) for sampling and analysis.

REFERENCES

1) J. Herbertson *et. al.*, in Steelmaking Conf. Proceedings, **74**, eds., ISS, Warrendale, PA, (1991), 171-185.
2) S. Yokoya *et. al.*: *ISIJ Int.*, (1994), **34**(11), 889.
3) S. Yokoya *et. al.*: *ISIJ Int.*, (1994), **34**(11), 883.
4) S. Yokoya *et. al.*: *ISIJ Int.*, (1998), **38**(8), 827.
5) S. Yokoya *et. al.*: *ISIJ Int.*, (1998), **38**(10), 1086.
6) O. Nomura: *Seramikkusu (Ceramics Japan: Bulletin of the Ceramic Spcoety of Japan)*, (2000), **35**(8), 617.
7) S. Yokoya *et. al.*, in Steelmaking Conference Proceedings, **79**, eds., ISS, Warrendale, PA, Pittsburgh, PA, (1996), 217-224.
8) N. Tsukamoto *et. al.*: *Taikabutsu*, (1994), **46**(4), 215.

9) N. Tsukamoto *et. al.*, in 74th Steelmaking Conference Proceedings, **74**, eds., ISS, Warrendale, PA, (1991), 803-808.
10) L. Zhang and B. G. Thomas, in Steelmaking National Symposium Mexico, eds., Morelia, Mich, Mexico, (2003),
11) K. Morward *et. al.*, in ISSTech2003, eds., ISS, Warrandale, PA, (2003), 1135-1155.
12) M. R. Ozgu *et. al.*, in ISSTech2003, **Electric Furnace, Steelmaking**, eds., ISS, Warrandale, PA, (2003), 31-40.
13) P. D. King *et. al.*, in ISSTech2003 Conference Proceedings, **Electric Furnace and Steelmaking**, eds., ISS, Warrandale, PA, (2003), 265-282.
14) J. Szekely and V. Stanek: *Metall. Trans.*, (1970), **1**(1), 119.
15) M. Yao *et. al.*: *Transactions of the Iron and Steel Institute of Japan*, (1984), **24**(2), s211.
16) B. G. Thomas *et. al.*: *Metall. Trans. B*, (1990), **21B**(2), 387.
17) X. Huang and B. G. Thomas: *Metall. Trans.*, (1993), **24B**(2), 379.
18) X. Huang and B. G. Thomas: *Metall. Trans. B*, (1996), **27B**(4), 617.
19) B. G. Thomas *et. al.*: *International Symposium on Cutting Edge of Computer Simulation of Solidification and Processes*, I. Ohnaka,eds., ISIJ, (1999), 113-128.
20) B. G. Thomas *et. al.*: *ISIJ Int.*, (2001), **41**(10), 1262.
21) K. I. Afanaseva and T. P. Iventsov: *Stal*, (1958), **18**(7), 599.
22) J. Szekely and R. T. Yadoya: *Metall. Trans. B*, (1972), **3**(5), 2673.
23) L. J. Heaslip *et. al.*: *Iron and Steelmaker (ISS Transactions)*, (1987), **14**(8), 49.
24) H. Tanaka *et. al.*: *Tetsu-to-Hagane*, (1992), **78**(5), 761.
25) T. Teshima *et. al.*: *Tetsu-to-Hagane*, (1993), **79**(5), 576.
26) D. Gupta and A. K. Lahiri: *Metall. Mater. Trans. B*, (1996), **27B**(5), 757.
27) L. J. Heaslip and J. Schade: *Iron and Steelmaker (ISS Transactions)*, (1999), **26**(1), 33.
28) M. Iguchi *et. al.*: *ISIJ Int.*, (2000), **40**(7), 685.
29) P. H. Dauby *et. al.*: *Rev. Met.*, (2001), **98**(4), 353.
30) J. Yoshida *et. al.*: *Tetsu-to-Hagane*, (2001), **87**(8), 529.
31) P. H. Dauby *et. al.*, in 73rd Steelmaking Conference Proc., **73**, eds., ISS, Warrendale, PA, (1990), 33-39.
32) M. B. Assar *et. al.*, in Steelmaking Conference Proceedings, **83**, eds., ISS, Warrendale, PA, (2000), 397-411.
33) P. H. Dauby and S. Kunstreich, in ISSTech2003, eds., ISS, Warrandale, PA, (2003), 491-503.
34) R. H. M. G. Nabben *et. al.*: *Ironmaking Steelmaking*, (1998), **25**(5), 403.
35) B. Grimm *et. al.*: *Steel Res.*, (1999), **70**(10),
36) B. Grimm *et. al.*: *Stahl und Eisen*, (1995), **115**(2), 71.
37) M. Yemmou *et. al.*: *Journal of Crystal Growth*, (1993), **128**(4), 1130.
38) J. K. Kim and P. K. RRRohatgi: *Metall. & Mater. Trans. B*, (1998), **29A**(1), 351.
39) D. M. Stefanescu and A. V. Catalina: *ISIJ Int.*, (1998), **38**(5), 503.
40) B. G. Thomas *et. al.*, in Steelmaking Conference Proceedings, **80**, eds., ISS, Warrendale, PA., (1997), 375-384.
41) R. C. Sussman *et. al.*, in 10th Process Technology Conference Proc., **10**, eds., Iron and Steel Society, Warrendale, PA, Toronto, Canada, April 5-8, 1992, (1992), 291-304.
42) M. R. Aboutalebi *et. al.*: *Metall. Mater. Trans. B*, (1995), **26B**(4), 731.
43) S. Asai and J. Szekely: *Ironmaking Steelmaking*, (1975), **3**(3), 205.
44) Y. Ho *et. al.*: *ISIJ Int.*, (1994), **34**(3), 255.
45) Y. Ho and W. Hwang: *ISIJ Int.*, (1996), **36**(8), 1030.
46) FLUENT5.1: Fluent Inc., Lebanon, New Hampshire, Report No., (2000).
47) B. E. Launder and D. B. Spalding: *Computer Methods in Applied Mechanics and Engr*, (1974), **13**(3), 269.
48) L. Zhang *et. al.*, in ISSTech2003, eds., ISS, Warrandale, PA, (2003), 141-156.
49) J. Lait *et. al.*: *Ironmaking Steelmaking*, (1974), **2**, 90.